Transport in Porous Media
https://doi.org/10.1007/s11242-020-01514-w

Numerical Simulation of the Physical–Chemical–Thermal Processes During Hydration Reaction of the Calcium Oxide/Calcium Hydroxide System in an Indirect Reactor

Mengyi Wang[1] · Li Chen[1] · Yuhao Zhou[2] · Wen-Quan Tao[1]

Received: 1 August 2020 / Accepted: 13 November 2020

Abstract
The $CaO/Ca(OH)_2$ thermochemical energy storage system can store heat through reversible reactions for long term and transport energy for long distance, and thus can solve the mismatching between energy supply and demand. In this study, a one-dimensional model is developed for the physical–chemical–thermal processes during the hydration reaction of $CaO/Ca(OH)_2$ system in an indirect fixed bed reactor, and the corresponding governing equations are solved by the tridiagonal matrix method with self-developed program parallelized by Message Passing Interface. The characteristics and complicated coupling mechanisms of the vapor flow, heat transfer, mass transport and reaction processes are analyzed. Then effects of inlet pressure, convective heat transfer, reactant porosity, reactant permeability and reactor size on the reaction performance are discussed, respectively. It is found that higher inlet pressure, heat transfer coefficient, permeability and porosity can enhance the heat and mass transfer processes, thus accelerating the reaction efficiently. Finally, the reaction performance under different conditions is comprehensively evaluated by four indicators including the reaction time, average power, temperature plateau duration and standard deviation.

Keywords Thermochemical energy storage · Hydration reaction · Indirect reactor · Heat and mass transfer

List of Symbols

Latin symbols

c	Reactant concentration (mol m^{-3})
c_p	Heat capacity (J kg^{-1} K^{-1})
D	Diameter of reactor (m)
D_p	Reactant particle diameter (m)

✉ Li Chen
lichennht08@mail.xjtu.edu.cn

[1] Key Laboratory of Thermo-Fluid Science and Engineering of MOE, School of Energy and Power Engineering, Xi'an Jiaotong University, Xi'an 710049, Shaanxi, China

[2] Huadian Electric Power Research Institute Co., Ltd, Hangzhou 310030, China

H	Height of reactor (m)
K	Reaction rate coefficient (s^{-1})
k	Permeability (m^2)
M	Mole mass (kg mol^{-1})
p	Vapor pressure (Pa)
P	Volume average power (W m^{-3})
R_g	Mole gas constant (J mol^{-1} K^{-1})
T	Temperature of reactor (K)
X	Reaction extent

Greek symbols

ε	Porosity of reactant
λ	Thermal conductivity (W m^{-1} K^{-1})
μ	Dynamic viscosity (Pa s)
ρ	Density (kg m^{-3})
Ψ	Volume energy density (kJ m^{-3}

Subscripts

CaO	Reactant CaO
$Ca(OH)_2$	Reactant $Ca(OH)_2$
eff	Effective
eq	Equilibrium
ini	Initial value
solid	Solid reactant and product
vapor	Reactant vapor

1 Introduction

Utilization of renewable energy, such as solar energy, wind energy and tidal energy, is limited by their intrinsically seasonal and regional discontinuity (Yadav and Banerjee 2016; Wood 2020; Yu et al. 2018). The supply and demand of renewable energy are time and space unmatched (Carrillo et al. 2019; Xu et al. 2014). Energy storage can eliminate such mismatching and can coordinate the energy supply and demand (Pardo et al. 2014b; Sunku Prasad et al. 2019). The thermochemical energy storage is based on reversible reactions where the forward and backward reactions release and absorb heat, respectively. The energy density of most of the reversible reaction systems is several times higher than the sensible and latent thermal storage method (Pan and Zhao 2017; Pardo et al. 2014b). Besides, the thermochemical energy storage has high efficiency (Sebarchievici 2018; Sunku Prasad et al. 2019; Pardo et al. 2014b; Herrmann and Kearney 2002). If the reactants are well separated, the thermal energy stored in reactants can be preserved for a long time without heat loss. These advantages allow the thermochemical system to store energy for long term and transport energy for long distance (Kugeler et al. 1975), rendering the thermochemical storage with the capacity to solve to a great extent the temporal and spatial mismatching between energy supply and demand.

Among various thermochemical systems based on different types of reversible reactions (Sunku Prasad et al. 2019), the calcium oxide/calcium hydroxide ($CaO/Ca(OH)_2$) system has high energy density of 364 kWh m^{-3} with reaction temperature in the range of 400 °C

to 600 °C (Pardo et al. 2014b). Besides, the reactants $CaO/Ca(OH)_2$ are inexpensive and convenient without virulence and risks of environment. Further, the water vapor can be easily separated from the $CaO/Ca(OH)_2$ solid particles through condensation without complex compression and can be stored at room temperature. Therefore, this system has drawn increasing attention. The reversible reactions of the $CaO/Ca(OH)_2$ system are as follows

$$CaO\ (s)\ +\ H_2O\ (g) \rightleftharpoons Ca(OH)_2(s) \quad \Delta H\ =\ -101.4\ \mathrm{kJ} \times \mathrm{mol}^{-1} \tag{1}$$

In Eq. (1), the forward reaction is the exothermic hydration reaction and the backward reaction is the endothermic dehydration reaction. In the dehydration process, the solid reactant $Ca(OH)_2$ is heated over the equilibrium temperature, either by the electrical heating or by the high-temperature heat transfer fluid (HTF), to produce the water vapor and CaO. In the hydration process, the preheated water vapor is imported into the reactor and then reacts with the solid reactant CaO to generate $Ca(OH)_2$. There are different types of reactors for the $CaO/Ca(OH)_2$ system depending on different criteria. Firstly, based on whether the solid reactants flow with the gas phase reactant or not, the reactors can be classified as fixed and fluid bed reactors. Secondly, based on whether the HTF contacts with the solid reactant directly or not, the reactors can be classified as direct and indirect reactors. The indirect (direct) type reactor can be a fixed or fluid bed reactor.

There have been several experimental studies of performance of $CaO/Ca(OH)_2$ system and the related reactive transport processes. Schaube et al. (Schaube et al. 2013a) experimentally studied the hydration and dehydration processes of the $CaO/Ca(OH)_2$ system for 25 cycles in a laboratory-scale direct fixed bed reactor. The reactant diameter was measured, and the increase in diameter was identified indicating the occurrence of the agglomeration of reactants. Due to its low permeability, the agglomerate was not accessible to the water vapor, and thus, it was not desirable for the reactions. The indirect fixed reactors were designed on the base of single heat exchanger plate (Schmidt et al. 2014, 2017; Roßkopf et al. 2015; Schmidt and Linder 2017; Linder et al. 2014). Two thin plate reactors with grooves filled by solid reactants were set symmetrically on two sides of the HTF channel. The charging and discharging processes were experimentally investigated at low pressure between 1.4 kPa and 20 kPa (Schmidt et al. 2017). In another study (Schmidt and Linder 2017), reaction processes in wider pressure range from 4 to 470 kPa were investigated. It was found that under higher pressure, the operation temperature of hydration and dehydration reactions was very close to the equilibrium temperature. Very recently, Mejia et al. (Cosquillo Mejia et al. 2020) have experimentally studied the reaction processes in an indirectly heated moving bed reactor. The unmodified ceramic encapsulated and Al_2O_3 encapsulated $Ca(OH)_2$ granules flowed inside the tubes, while the HTF flowed around the tubes on the shell side. The results showed that after sixfold cycles, the ceramic shell granules flowed freely; however, the reaction performance and the conversion were reduced.

Numerical simulations have also been implemented to study the complicated processes taking place in $CaO/Ca(OH)_2$ system (Nagel et al. 2013; Shao et al. 2013). Due to the multiple physical–chemical–thermal processes, as well as the complicated operating conditions and porous structures involved, it is really challenging to develop corresponding numerical models. The hydration/dehydration reactions in a direct fixed bed reactor were modeled with an axisymmetric two dimension (2D) model by Schaube et al. (Schaube et al. 2013b). The Darcy's law with Kozeny–Carman equation for the porosity–permeability relationship was utilized to describe the fluid flow. The heat transfer between gas and solid reactants as well as the radiation between side wall and solid reactants were taken into account. Further, the dehydration and hydration processes in an indirect fixed bed reactor consisted of

eleven thin plates were numerically studied in a 3D model (Ranjha and Oztekin 2017). The results showed that the reaction in low-porosity bed was time and space heterogeneous.

The simulation in 2D and 3D models can provide detailed information about the reactive properties. When the $CaO/Ca(OH)_2$ thermochemical reactor is a part of an energy utilization and conversion system, and if studies are conducted at the scale of the entire reactor, it is impossible to resolve the details of the heat and mass transfer processes inside the reactors. Thus, the models need to be simplified to one-dimensional (1D) or even zero-dimensional model to catch the important characteristics inside the reactor and suit the requirements for engineering applications (Shao et al. 2013).

Darkwa et al. (Darkwa et al. 2006) developed a 1D model to study the hydration process of the $CaO/Ca(OH)_2$ system in a direct fluid bed reactor. The fluid flowed at a constant velocity to keep the solid particles suspended in the gas flow. It was found that the velocity of gas phase had significant influence on the reaction processes. Recently, Seitz et al. (Seitz et al. 2020) have proposed a 1D model to consider the variation of the solid volume fraction before and after reactions (0.8 for CaO and 0.6 for $Ca(OH)_2$). Accordingly, the permeability also changed as the porosity varied. The change of porosity affected the energy density and source terms in governing equations, while the change of permeability had influence on fluid flow leading to different pressure distributions.

From the above review, it can be concluded that the physical–chemical–thermal processes in hydration/dehydration reaction of the $CaO/Ca(OH)_2$ system are very complicated. The corresponding heat and mass transfer processes should be further enhanced to improve the reaction performance. Effects of different operating and structural parameters on the heat and mass transfer processes as well as the reactor performance still require further investigation. Therefore, in the present study, the hydration process of the $CaO/Ca(OH)_2$ system in an indirect fixed bed reactor is numerically studied. The remaining parts of this work are as follows. In Sect. 2, a 1D model taking into account the physical–chemical–thermal processes is developed and discussed. In Sect. 3, the characteristics and interaction effects of heat and mass transfer during reactive process for the base case are analyzed in detail. Then the influence of operating conditions and structural parameters on the hydration reaction is investigated and discussed. At last, four indicators, namely the energy density, average power, temperature plateau and standard deviation, are adopted to evaluate the reaction performance under different conditions.

2 Physical–Chemical–Thermal Model

As shown in Fig. 1, the hydration process is studied in an indirect fixed reactor with cylinder shape. The length and diameter of the reactor are 0.24 m and 0.08 m, respectively. The reactant is packed inside the reactor and the heat transfer fluid flows outside the reactor. One side of the reactor is for water vapor to flow in, and the other side is sealed surface. Such structure was widely adopted in the literature (Schmidt et al. 2014; Ranjha and Oztekin 2017; Pan and Zhao 2017). The heat released by the hydration reaction is removed by the HTF outside the reactor through convective heat transfer. The cylinder reactor is simplified into a 1D domain with the axial direction reserved. As shown in Fig. 1, the red end point on the left represents the water vapor inlet surface and the blue end point on the right represents the sealed bottom wall surface. Five observation points [A (0.002), B (0.06), C (0.12), D (0.18) and E (0.238)] are selected in the reactor to analyze the evolution of key parameters.

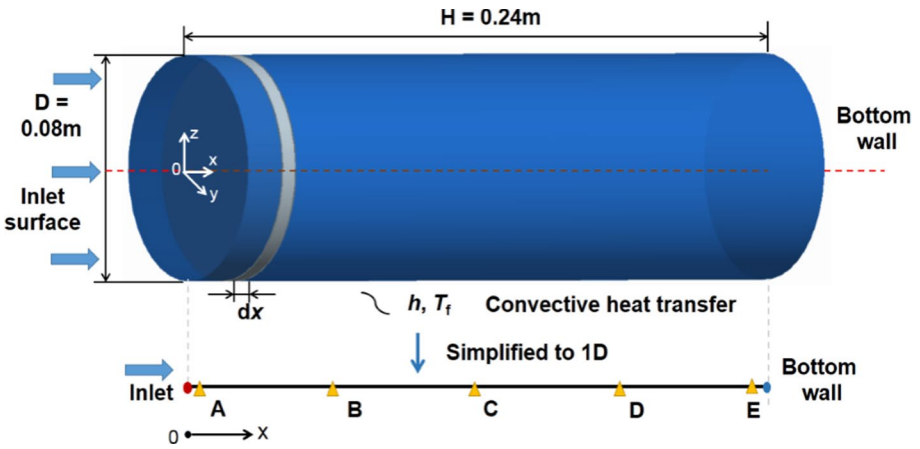

Fig. 1 Schematic of the simplification of reactor: the boundary conditions and five observation points

To establish the physical–chemical–thermal model, the following assumptions are employed:

(1) The water vapor is considered as ideal gas.
(2) The porosity, particle diameter and thermal conductivity of the solid reactants are kept constant during the hydration processes.
(3) The local thermal equilibrium hypothesis is employed for the heat transfer process between the solid reactants and the water vapor.
(4) The thermal contact resistance between the reactant particles and the reactor wall is ignored.
(5) When reaction extent of the calculation district reaches 0.99, the hydration is considered to be complete and the local reaction rate is set as zero.

2.1 Physical–Chemical–Thermal Model and Governing Equations

During the hydration reaction, the solid reactant CaO absorbs water vapor and generates $Ca(OH)_2$ along with release of heat according to Eq. (1). The hydration reaction obeys the following equilibrium equation (Schaube et al. 2012)

$$\ln\left(\frac{p}{10^5}\right) = -\frac{12845}{T_{eq}} + 16.508 \tag{2}$$

When the temperature is below the equilibrium temperature T_{eq} at a certain vapor pressure p, the exothermic hydration reaction is activated. Conversely, when the temperature is higher than the equilibrium temperature, the endothermic dehydration reaction takes place. In the present study, the initial conditions are set in such way that the hydration reaction is activated as will be introduced in 2.2.

The hydration reaction consumes the CaO and generates $Ca(OH)_2$, and the conversion of the reactant molar concentration c is as follows

$$\frac{\partial c_{\mathrm{CaO}}}{\partial t} = -K \cdot c_{\mathrm{CaO}} \tag{3}$$

where K is the reaction rate coefficient. It is affected by temperature T, pressure p and the reaction extent X, and can be calculated by the following expression (Schaube et al. 2012)

$$\begin{aligned} K &= 13945 \times \exp\left(\frac{-89.486 \times 10^3}{R_{\mathrm{g}} T}\right) \cdot \left(\frac{p}{p_{\mathrm{eq}}} - 1\right)^{0.83} \cdot 3(1-X) \times [-ln(1-X)]^{0.666}, \quad T_{\mathrm{eq}} - T \geq 50\ \mathrm{K} \\ K &= 1.0004 \times \exp\left(\frac{53.332 \times 10^3}{T}\right) \cdot \left(\frac{p}{10^5}\right)^6 \cdot (1-X), \quad 0\ \mathrm{K} < T_{\mathrm{eq}} - T < 50\ \mathrm{K} \end{aligned} \tag{4}$$

where R_{g} is the ideal gas constant. The reaction extent is defined as the fraction of CaO consumed

$$\frac{\mathrm{d}X}{\mathrm{d}t} = 1 - \frac{c_{\mathrm{CaO}}}{c_{\mathrm{CaO},ini}} \tag{5}$$

where $c_{\mathrm{CaO,ini}}$ is the initial molar concentration of CaO depending on the porosity ε and mass density ρ_{CaO}

$$c_{\mathrm{CaO,\ ini}} = \frac{\rho_{\mathrm{CaO}}}{M_{\mathrm{CaO}}} \cdot (1-\varepsilon) \tag{6}$$

where M_{CaO} is the molar mass of CaO.

In previous experimental investigations, it was found that the reactants are porous media formed by accumulation of tiny solid particles with diameter in micron scale. Therefore, the theory of transport phenomena in porous media is adopted to establish the governing equations of physical–chemical–thermal processes in the reactor. The mass conservation equation of the water vapor is as follows

$$\frac{\partial \rho_{\mathrm{g}}}{\partial t} + \nabla(u\rho_{\mathrm{g}}) = q_{\mathrm{m}} \tag{7}$$

$$q_{\mathrm{m}} = -M_{\mathrm{vapor}} \cdot K \cdot c_{\mathrm{CaO}} \tag{8}$$

where M_{vapor} is the molar mass of water vapor and u is the superficial velocity. The mass source term is determined by the reaction rate coefficient K as well as the molar concentration of CaO.

The Darcy equation and Kozeny–Carman equation have been verified which can describe the flow of water vapor in $Ca(OH)_2$ particles and the relationship between permeability, particle diameter and porosity (Schaube et al. 2013a; Darcy 1956)

$$u = -\frac{k}{\mu}\nabla p \tag{9}$$

where k is the permeability of porous reactant equation

$$k = \frac{D_{\mathrm{p}}^2 \varepsilon^3}{180(1-\varepsilon)} \tag{10}$$

where D_{p} is the particle diameter of the CaO.

Based on the local thermal equilibrium hypothesis, the energy conservation equation is as follows

$$\frac{\partial((\rho c_{\mathrm{p}})_{\mathrm{eff}}T)}{\partial t}+\varepsilon\frac{\partial((\rho c_{\mathrm{p}}u)_{\mathrm{vapor}}T)}{\partial t}=\frac{\partial}{\partial x}\left(\lambda_{\mathrm{eff}}\frac{\partial T}{\partial x}\right)+\Phi_{\mathrm{thermal}} \tag{11}$$

where c_{p} and λ are specific heat and thermal conductivity of reactants, respectively. The volume changing work caused by change of gas density (Seitz et al. 2020) is less than 10% of the thermal power and 1% of the energy stored (Schaube 2011), and thus is ignored in the present study. The effective physical parameters in the above equations take the effects of porosity into account

$$(\rho c_p)_{eff}=\varepsilon\cdot(\rho c_p)_{\mathrm{vapor}}+(1-\varepsilon)\cdot(\rho c_p)_{\mathrm{solid}} \tag{12}$$

$$\lambda_{eff}=\varepsilon\cdot\lambda_{\mathrm{vapor}}+(1-\varepsilon)\cdot\lambda_{\mathrm{solid}} \tag{13}$$

As the reaction proceeds, the composition of the solid reactants changes, and thus, the physical parameters of solid reactant change accordingly

$$(\rho c_{\mathrm{p}})_{solid}=X\cdot(\rho c_{\mathrm{p}})_{\mathrm{Ca(OH)_2}}+(1-X)\cdot(\rho c_{\mathrm{p}})_{\mathrm{CaO}} \tag{14}$$

$$\lambda_{solid}=X\cdot\lambda_{\mathrm{Ca(OH)_2}}+(1-X)\cdot\lambda_{\mathrm{CaO}} \tag{15}$$

Considering the high level of the reactant temperature, the change of heat capacities should be considered (Ranjha and Oztekin 2017)

$$c_{p,\,\mathrm{CaO}}=0.1643T+799.15 \tag{16}$$

$$c_{p,\mathrm{Ca}(OH)_2}=0.3829T+1218.87 \tag{17}$$

In Eq. (11), Φ_{thermal} is the energy source term calculated by the following equation

$$\Phi_{\mathrm{thermal}}=\Phi_{\mathrm{reac}}+\Phi_{\mathrm{conv}}=K\cdot c_{\mathrm{CaO}}\cdot\Delta H+\frac{4h}{D}(T_{\mathrm{f}}-T) \tag{18}$$

The first term and second term on the right-hand side are the heat released during the exothermic hydration reaction and the heat removed by the convective heat transfer outside the reactor wall, respectively. The second term is explained in detail as follows. For 1D simulation in the present study, the amount of convection heat at the side wall is converted into a source term in the energy conservation equation. In the 3D cylinder reactor, for a small control volume along the x direction with height of dx as shown in Fig. 1, the total convection heat at the wall can be calculated by

$$Q_{\mathrm{conv}}=h\cdot A\cdot(T_{\mathrm{f}}-T)=h(\pi D\cdot\mathrm{d}x)(T_{\mathrm{f}}-T) \tag{19}$$

where h is the convective heat transfer coefficient and T_{f} is the temperature of the HTF. Since the volume of the element is as follows

$$V=\frac{\pi D^2}{4}\mathrm{d}x \tag{20}$$

the convective source term is determined by

$$\Phi_{\text{conv}} = \frac{Q_{\text{conv}}}{V} = \frac{4h}{D}(T_{\text{f}} - T) \tag{21}$$

It is worth mentioning that the simplification from 3 to 1D ignores the heat and mass transfer processes in the radial direction. Although such 1D model requires few computational resources and is efficient for fast prediction, we have to admit that such simplification may lead to deviation due to the low thermal conductivity and permeability of reactants.

The above equations describe the physical–chemical–thermal processes during the $CaO/Ca(OH)_2$ hydration reaction. Central difference, second-order upwind and implicit scheme are adopted to discretize the diffusion term, the convection term and the unsteady term, respectively. The tridiagonal matrix method (TDMA) is adopted to solve the discretized equations with the self-developed program parallelized by Message Passing Interface (MPI). The equations are solved in the following order. The governing equations of the reaction kinetic (Eq. (3)) are solved firstly. Then the mass conservation equation (Eq. (7)) and the Darcy equation (Eq. (9)) are solved simultaneously with the ideal gas hypothesis. At last, the energy conservation equation (Eq. (11)) is solved based on the velocity obtained. The simulation is terminated when the hydration reaction is completed.

2.2 Initial and Boundary Conditions

For the base case, initially, the reactor is filled by solid reactant CaO with porosity of 0.8 and water vapor of which the pressure is 101,325 Pa and temperature is 393 K, which can ensure the occurrence of the hydration reaction. At the left inlet, saturated water vapor is supplied into the domain with pressure of 200,000 Pa and temperature of 393 K. The right bottom is set as sealed adiabatic wall. Note that in Sect. 3.7, the right surface is also changed into an open outlet, and the fully developed boundary condition is employed for the open outlet. Finally, for the convection heat transfer around the side wall, the HTF is at constant temperature 293 K and the convective heat transfer coefficient is 100 W (m^{-2}

Table 1 Physical parameters of reactants and reaction conditions

Symbol	Parameter	Value
D_{p}	Diameter of reactant	5 μm
M_{CaO}	Mole mass of CaO	0.056 kg mol^{-1}
M_{vapor}	Mole mass of vapor	0.018 kg mol^{-1}
p_{ini}	Initial pressure	101,325 Pa
p_{in}	Inlet pressure	200,000 Pa
T_{f}	Heat transfer fluid temperature	293 K
T_{ini}	Initial temperature	393 K
T_{in}	Inlet temperature	393 K
ε	Porosity of reactant	0.8
λ_{solid}	Thermal conductivity of solid reactant	2 W m^{-1} K^{-1}
ρ_{CaO}	Density of CaO	3320 kg m^{-3}
$\rho_{\text{Ca(OH)2}}$	Density of $Ca(OH)_2$	2200 kg m^{-3}

K^{-1}), which represents the forced air-cooling condition. Values of other parameters are listed in Table 1.

2.3 Temporal and Spatial Independence

Based on the above governing equations and the conditions, the hydration process is simulated by adopting different time and space steps to verify the temporal and spatial independence. The temperature of point B with different time and space steps is shown in Fig. 2. The curves of cases with the time step and space step of 1×10^{-4} s, 1×10^{-4} m and 1×10^{-5} s, 1×10^{-4} m are in good coincidence with negligible error. Thus, the time step of 1×10^{-4} s and space step of 1×10^{-4} m are adopted in the following simulation.

3 Results and Discussion

3.1 The Base Case

Based on the initial and boundary conditions of the base case described in Sect. 2.2, the distribution and time evolution of the reaction extent, temperature, pressure and velocity of the base case are displayed in Figs. 3, 4, 5 and 6. The total reaction time is 1500 s when the reaction extent in the reactor reaches 0.99. As shown in Fig. 3a, the reaction extent of points A to E rises successively, indicating the reaction proceeds from the left inlet to the right bottom. As time increases, the reaction extent curves of points A to C first increase sharply, and then, the increase rate slows down. The curve of point D keeps a low value before 400 s, after which it starts to increase quickly, and then, the increase rate also declines. This is because at the early stage of the reaction (before

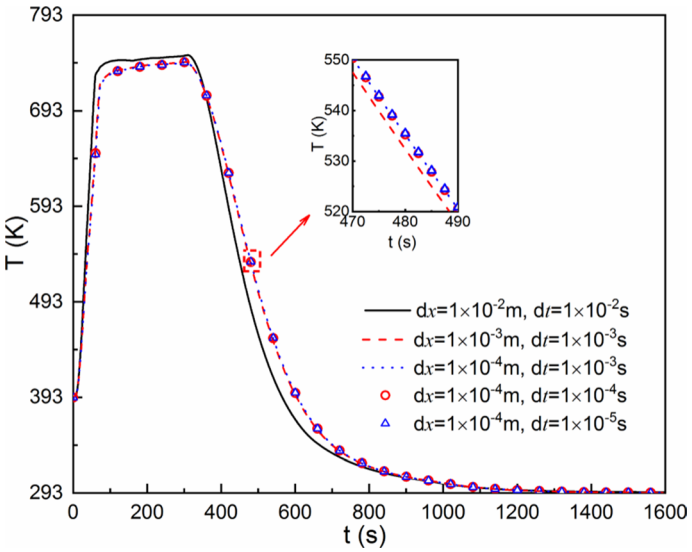

Fig. 2 Validation of space and time step independence: temperature of point B with different time and space steps

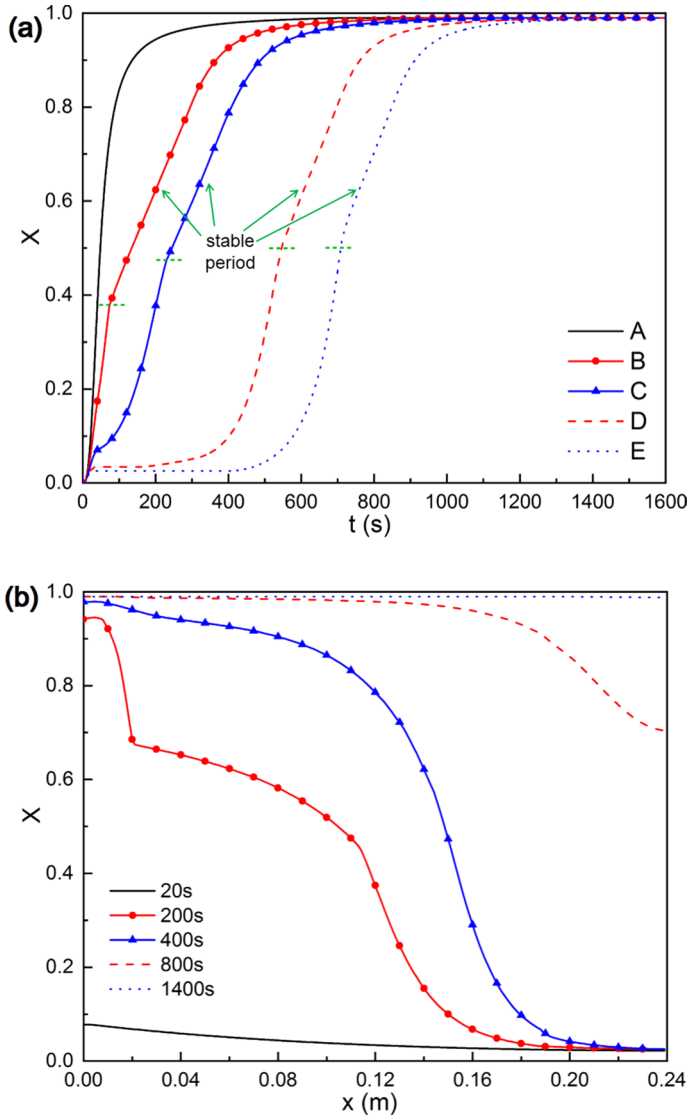

Fig. 3 Reaction extent of the base case. **a** Reaction extent evolution of different observation points; **b** reaction extent distribution in the entire reactor at different times

400 s), most of the water vapor is consumed by the hydration reaction in the upstream region corresponding to points A to C. Thus, point D in the downstream region is starved of water vapor leading to low local reaction extent. After 400 s, the hydration reaction in the upstream region is almost complete, and thus, the influent vapor is able to reach the downstream region and react with CaO inside the reactor. Therefore, the reaction extent of point D starts to rise quickly. The variation of reaction extent of point E falls behind that of D, and the changing trend can be explained similarly. Note that in

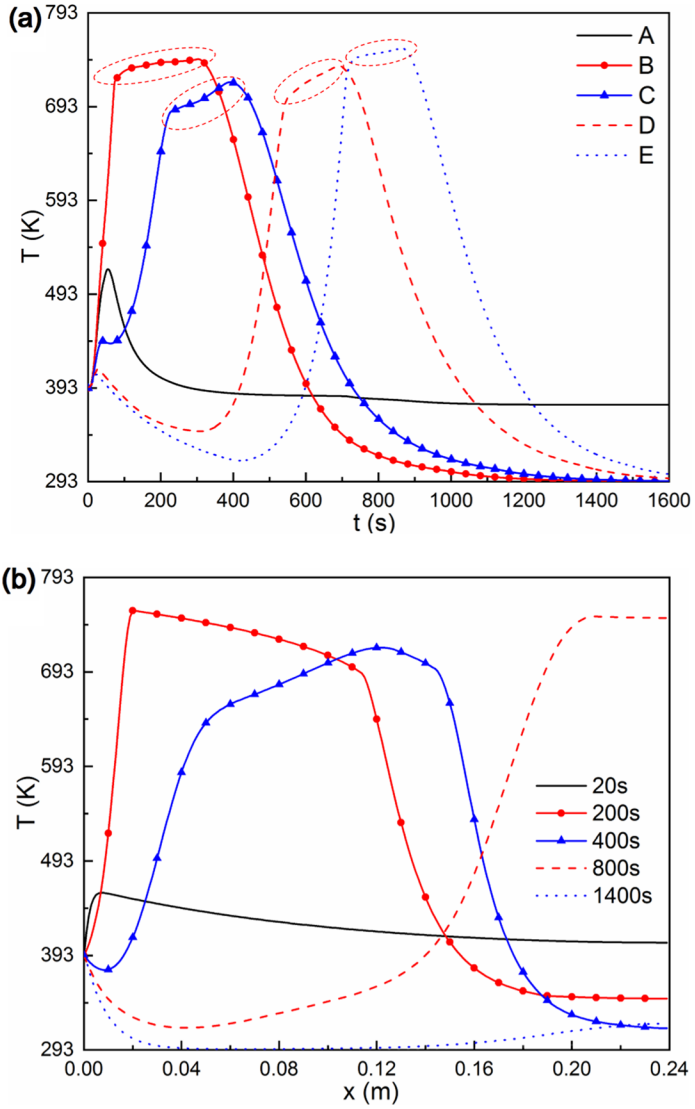

Fig. 4 Temperature of the base case. **a** Temperature evolution of different observation points; **b** temperature distribution in the entire reactor at different times

each curve especially that for points B to E, there are inflection points marked by the horizontal dotted green lines, after which the increase in the reaction extent undergoes a stable period. Such stable increase indicates locally stable reaction which is desirable.

The distribution of the reaction extent in the entire reactor at different times is further shown in Fig. 3b. At 20 s, the distribution in the entire region is uniform and is at very low level because a small quantity of water vapor exists in the reactor initially. Then, at 200 s and 400 s, only the reaction extent in the upstream region increases obviously because most of the water vapor is consumed by hydration reaction in this region.

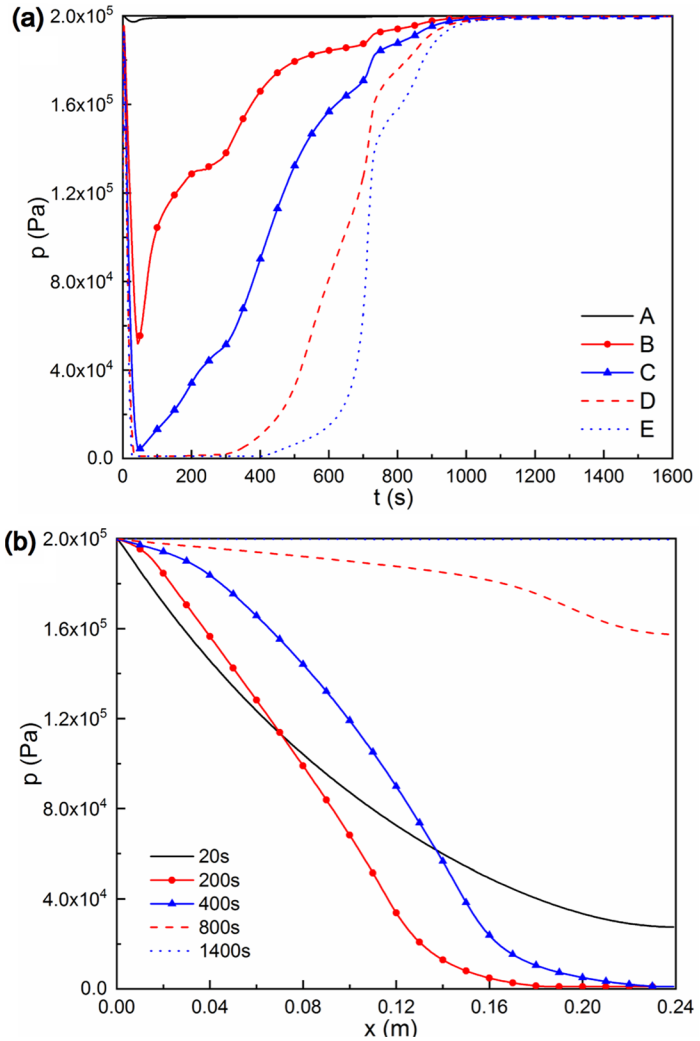

Fig. 5 Pressure of the base case. **a** Pressure evolution of different observation points; **b** pressure distribution in the entire reactor at different times

Especially at 200 s, hydration reaction in the region 0–0.02 m is almost complete and the rate of heat release is slow. The hydration in the region 0.02–0.12 m is at a stable and strong state with large amount of heat released. Thus, the reaction extent is lower and the corresponding temperature is high (see Fig. 4b). Meanwhile, hydration in the region 0.12–0.24 m is limited by lack of water vapor leading to low reaction extent and low temperature (see Fig. 4b). After 400 s, the reaction extent of the downstream region also rises significantly which is corresponding to the quick increase of curves of point D and point E in Fig. 3a.

The temperature of different observation points under different times is shown in Fig. 4 to more clearly understand the complex coupled physical–chemical–thermal

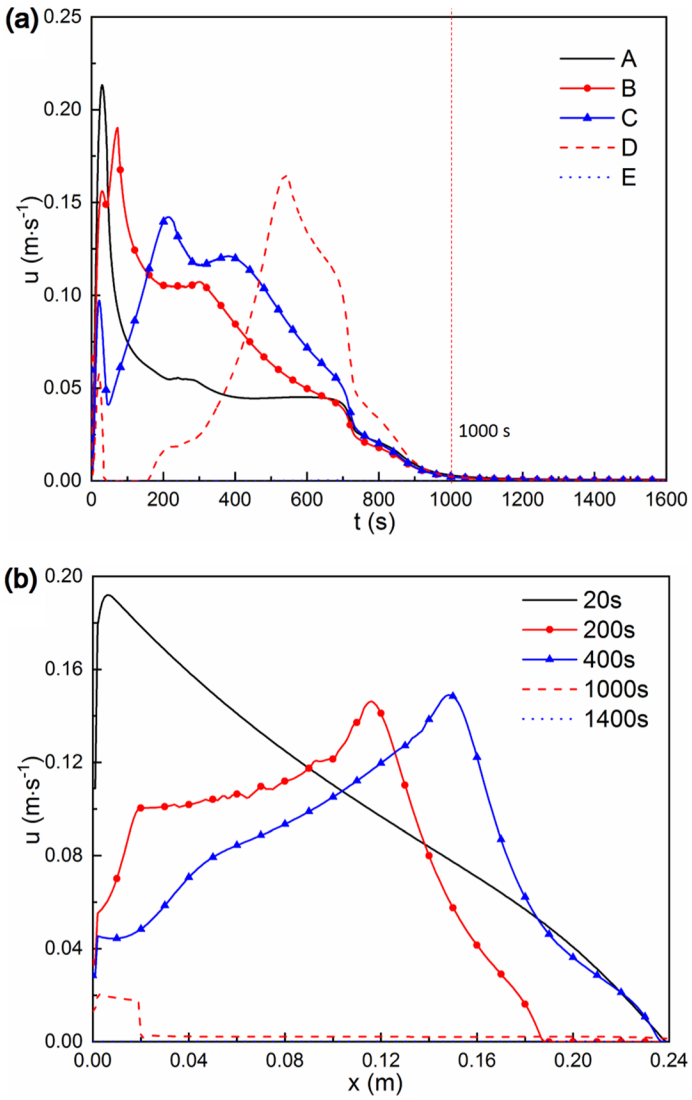

Fig. 6 Velocity of the base case. **a** Velocity evolution of different observation points; **b** velocity distribution in the entire reactor at different times

processes. In Fig. 4a, the temperature of observation points A to C first increases sharply due to the strong exothermic hydration reaction and then reaches a temperature plateau (marked by circles in Fig. 4a). The plateau period indicates the equilibrium between the heat release by the inner hydration reaction and the heat removed by the external convective heat transfer, which is corresponding to the stable reaction period after the turning points in Fig. 3a. After the plateau, the local exothermic hydration reaction becomes weak, and thus, the release of heat decreases, leading to drop of temperature. Specially, the temperature of point D and point E first declines for about 300–400 s.

This is because of the convective heat transfer outside the reactor as well as the sluggish inner exothermic reaction due to lack of the water vapor. After this initial period, the water vapor is adequate for hydration reaction and the variation of temperature of points D and E is similar to that of points A to C. Note that the temperature plateau of point A is much lower and shorter than other points, mainly because point A is close to the inlet and is significantly affected by the relatively low inlet temperature. In Fig. 4b, it can be found that the region of high temperature at different times moves from the inlet to the bottom due to migration of local exothermic reaction, in accord with the distributions of the reaction extent in Fig. 3. At 1400 s, the temperature in most region is close to the HTF temperature due to the completion of reaction. This is in accord with the physical fact.

To further verify the results in the present study, the temperature variations are compared with existing experimental results in the literature. Given the different types of reactors and operating conditions in different experiments, only qualitative comparison is allowed. The local temperature of points 1, 5, 11 and 13 in Fig. 8 of Ref. (Schmidt et al. 2014) in an indirect reactor increased due to onset of the exothermic hydration reaction. Then the high temperature maintained for some time when the reaction was at steady state, and then, it dropped due to completion of the hydration reaction. The temperature of point B in a direct fixed bed reactor during the hydration reaction in Figs. 8, 9 and 11 of Ref. (Yan and Zhao 2016) increased rapidly when the hydration reaction began and kept at a high level for a while. Since there was no heat transfer outside the reactor, the temperature of point B then decreased slowly. The temperature in Fig. 11 of Ref. (Pardo et al. 2014a) increased when the hydration reaction started and stayed at high level before it decreased. The changing trend of temperature in Fig. 4 in the present study agrees with the above experimental results (Pardo et al. 2014a; Schmidt et al. 2014; Yan and Zhao 2016).

Pressure variation of the base case is further displayed and discussed. As shown in Fig. 5a, the pressure of point A drops slightly due to consumption of water vapor by the hydration reaction and then recovers quickly due to supplement of vapor from the inlet. The pressure of points B and C first decreases to a relatively low value due to huge consumption of water vapor caused by the strong local hydration reaction. Then, as the hydration reaction proceeds, the consumption of water vapor at the upstream region slows down, leading to recovery of the pressure. Differently, the main reason of the relatively low pressure of points D and E before 400 s is the insufficient supply of water vapor as discussed previously. When the reaction in the upstream region is complete, the water vapor can penetrate deep into the reactor and thus renders recovery of the pressure. When the hydration reaction is terminated in the entire reactor, the water vapor fills the entire reactor and the pressure of all the five points are the same as the inlet pressure.

The pressure at different times is shown in Fig. 5b. It can be found that the curves of 20 s and 200 s intersect with each other. In the region before the intersection, the pressure at $t = 20$ s is lower than that at $t = 200$ s. The reason is that this region is closer to the inlet and hydration reaction in this region starts earlier leading to consumption of the vapor, and thus, the local pressure is lower. As time increases to 200 s, consumption of water vapor in this local region slows down causing the increase in the pressure. As the water vapor is consumed in the upstream region and is not efficiently provided to the region after the intersection, the pressure at $t = 200$ s is lower than that at $t = 20$ s. As time proceeds, pressure at the downstream region gradually increases. Finally, the entire domain is filled with water vapor at pressure of the inlet value. It should be mentioned that the inlet pressure is the highest pressure that can be reached in the reactor and the corresponding equilibrium

temperature is 793 K. Due to convection outside the reactor and the limited reaction, the highest temperature inside the reactor is below 793 K as shown in Fig. 4.

Finally, the velocity distribution of the base case is investigated. As shown in Fig. 6a, the region of high velocity moves from the inlet to the bottom indicating the advancement of reaction. The velocity after about 1000 s drops to almost zero due to little pressure gradient caused by recovery of the pressure. The distribution of velocity in Fig. 6b shows sharp drop at 200 s in the downstream region due to the small pressure gradient for lack of water vapor. Besides, at 1000 s and 1400 s, the velocity in the whole reactor is relatively low which is corresponding to the low velocity after 1000 s in Fig. 6a.

3.2 Effects of the Inlet Pressure

According to the reaction kinetics in Eq. (4), the pressure and temperature have direct effects on the reaction rate. In this section, the inlet pressure is varied from 200,000 Pa to 150,000 Pa, 300,000 Pa and 400,000 Pa, respectively. The inlet temperature is changed to the corresponding water vapor saturation temperature. Other conditions remain the same as the base case in Sect. 3.1.

The reaction time of cases with different inlet pressures is listed in Table 2. As the inlet pressure increases, the reaction time reduces due to greater pressure difference between the inlet and the inner region of the reactor. Higher pressure difference provides stronger

Table 2 Reaction time of cases with different conditions

Case	Conditions	Reaction time
Change the inlet pressure/temperature (base case-200000 Pa/393 K)	150,000 Pa/384 K	2000 s
	300,000 Pa/406 K	1000 s
	400,000 Pa/416 K	710 s
Change the convective heat transfer coefficient (base case-100 W m^{-2} K^{-1})	10 W m^{-2} K^{-1}	3970 s
	500 W m^{-2} K^{-1}	1100 s
	2000 W m^{-2} K^{-1}	980 s
Change the porosity of solid reactants (base case-0.8)	0.7	3690 s
	0.6	7820 s
	0.5	21,080 s
	0.4	73,960 s
Change the permeability of solid reactants (base case-2 × 10^{-12} m^2, D_p = 5 μm)	4 × 10^{-12} m^2, D_p = 7.5 μm	1206 s
	2 × 10^{-11} m^2, D_p = 17 μm	904 s
	2 × 10^{-10} m^2, D_p = 53 μm	884 s
	2 × 10^{-9} m^2, D_p = 168 μm	882 s
	2 × 10^{-8} m^2, D_p = 530 μm	882 s
Change the reactor length (base case-0.24 m)	0.96 m	5880 s
	0.48 m	2660 s
	0.12 m	970 s
Change the reactor diameter (base case-0.08 m)	0.04 m	1270 s
	0.16 m	1890 s
	0.32 m	2280 s
Change the boundary condition (base case-adiabatic wall)	Fully developed outlet	1800 s

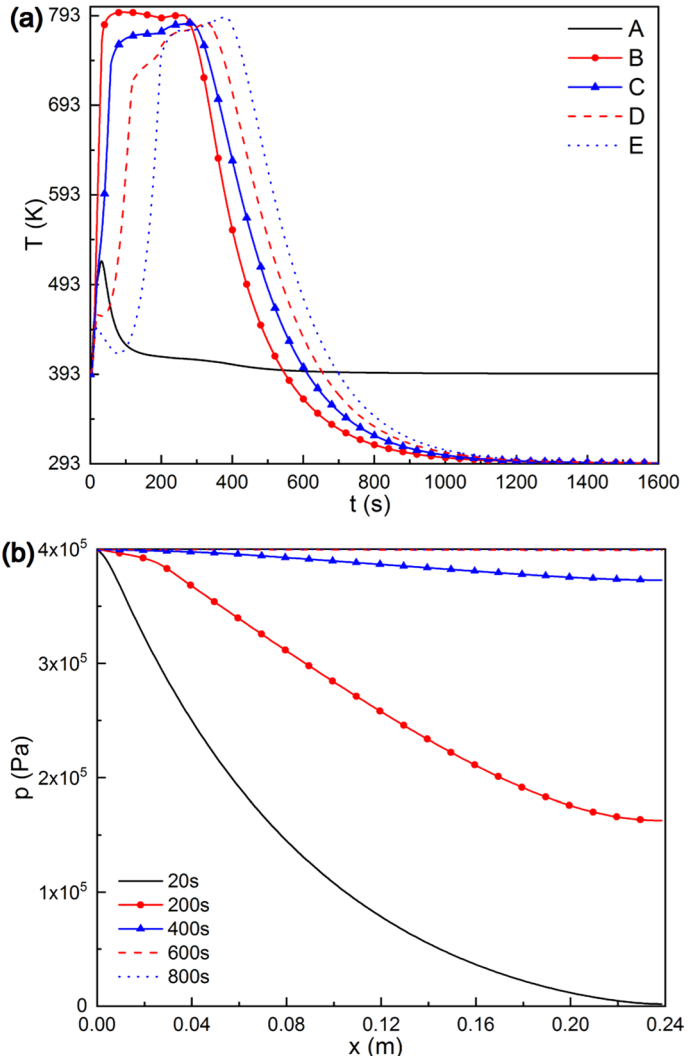

Fig. 7 Effects of the inlet pressure. **a** Temperature distribution of different observation points when the inlet pressure is 400,000 Pa; **b** pressure distribution in the entire reactor at different times when the inlet pressure is 400,000 Pa

driving force and facilitates the vapor flow. Thus, the water vapor can reach the downstream region faster and the hydration reaction can occur earlier. In addition, the increase in the inlet saturation temperature results in higher reaction rate coefficient according to Eq. (4), which also accelerates the hydration reaction.

Here, the distribution of temperature and pressure of different points with inlet pressure 400,000 Pa is analyzed. As shown in Fig. 7a, the temperature plateaus reach a higher level compared with the base case and the overlap of the temperature plateaus of different points is more obvious. This means as the inlet pressure increases, the hydration reaction takes place simultaneously and strongly, thus releasing more heat. Besides,

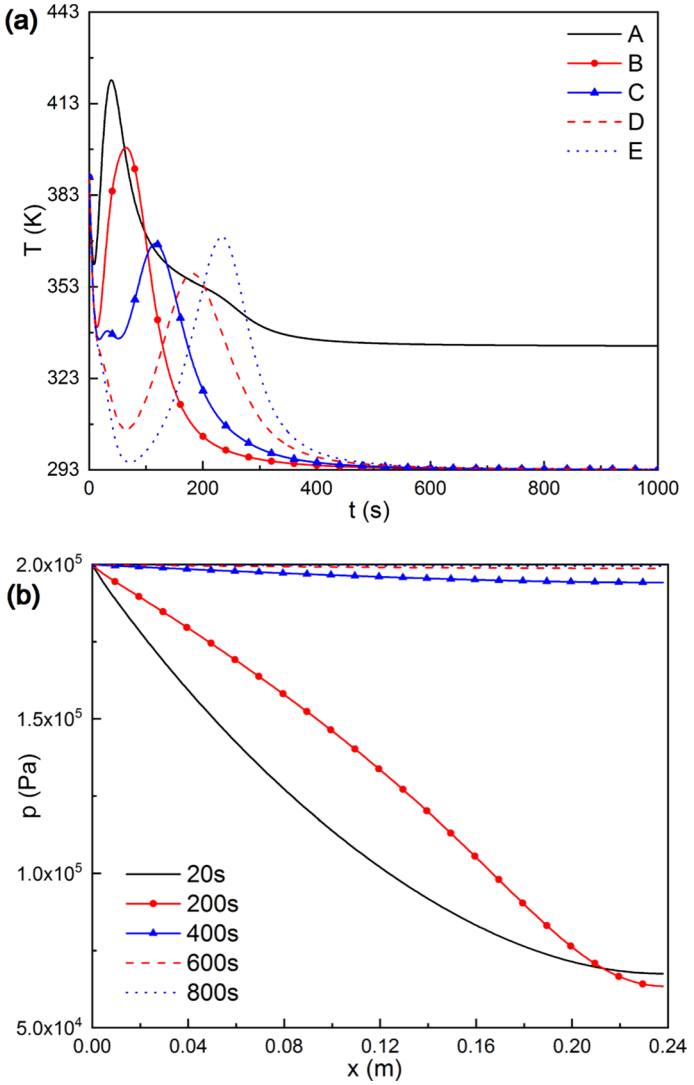

Fig. 8 Effects of the convective heat transfer coefficient. **a** Temperature distribution of different observation points when the heat transfer coefficient is 2000 Wm^{-2} K^{-1}; **b** pressure distribution in the entire reactor at different times when the heat transfer coefficient is 2000 W m^{-2} K^{-1}

as the inlet pressure increases, the maximum temperature achieved is also higher than the base case. The pressure distribution at different times in Fig. 7b shows that the pressure in the region far from the inlet can recover fast and there is no interaction between different curves. This means the flow of water vapor is promoted by higher pressure difference, and nowhere in the entire reactor, the hydration reaction is limited by a lack of water vapor.

Fig. 9 Effects of the reactant porosity. **a** Power and energy density of cases with different porosity; **b** temperature distribution of different observation points when the porosity is 0.4; **c** pressure distribution in the entire reactor at different times when the porosity is 0.4

3.3 Effects of the Convective Heat Transfer Coefficient

The convective heat transfer outside the reactor represents the remove rate of heat released by the hydration reaction, which has direct influence on the temperature distribution and thus affects the hydration reaction process. The convective heat transfer coefficient is varied from 100 W m^{-2} K^{-1} to 10 W m^{-2} K^{-1} (imitating the natural convection condition of air), 500 W m^{-2} K^{-1} (imitating the natural convection condition of water) and 2000 W m^{-2} K^{-1} (imitating the forced convection condition of water), respectively. Other conditions are the same as the base case. On the one hand, the stronger convective heat transfer can remove the heat of reaction more efficiently, thus pushing the reaction status away from the reaction equilibrium and facilitating the hydration reaction (Criado et al. 2014). On the other hand, the stronger convection also leads to lower temperature in the reactor, thus leading to slow reaction rate according to Eq. (4). As summarized in Table 2, the reaction time reduces as the convective heat transfer coefficient increases. Therefore, the positive effect of the enhanced convective heat transfer overwhelms the negative effect.

Figure 8 shows the temperature and pressure distributions in the domain with heat transfer coefficient of 2000 W m^{-2} K^{-1}. Compared with the base case, the level of the temperature plateau in Fig. 8a drops obviously and the duration of the temperature plateau becomes shorter, due to the timely remove of the reaction heat. As shown in Fig. 8b, the fast hydration reaction allows the water vapor to flow into the downstream region more quickly leading to faster recovery of the pressure.

3.4 Effects of the Reactant Porosity

Solid reactants $CaO/Ca(OH)_2$ are porous media formed by the accumulation of tiny particles. The reactant porosity is varied from 0.8 to 0.7, 0.6, 0.5 and 0.4, respectively, with the permeability changed according to Eq. (10) while keeping the particle diameter as constant. Other conditions are the same as the base case. In experiments (Schaube et al. 2013a; Schmidt et al. 2014, 2017), the porosity of initial reactant ranged from 0.5 to 0.8 depending on the infilling process. The porosity of solid reactants was assumed as 0.8 in most of the existing numerical studies (Schaube et al. 2013b; Ranjha and Oztekin 2017; Wang et al. 2019). The compressed solid reactant with lower porosity can acquire higher energy density, but also results in smaller pores of the reactant. As the porosity decreases, on the one hand, the amount of the solid reactant will increase proportionally requiring more reaction time for the completion of the hydration reaction. On the other hand, the decrease in the porosity leads to reduction in the permeability, causing higher flow resistance inside the reactor. As a result, the decrease in the porosity leads to significant increase in the reaction time as shown in Table 2.

The volume energy density is calculated by the following equation

$$\psi = (1-\varepsilon)\cdot\frac{\rho_{\mathrm{CaO}}}{\mathrm{M}_{\mathrm{CaO}}}\cdot\Delta H \tag{22}$$

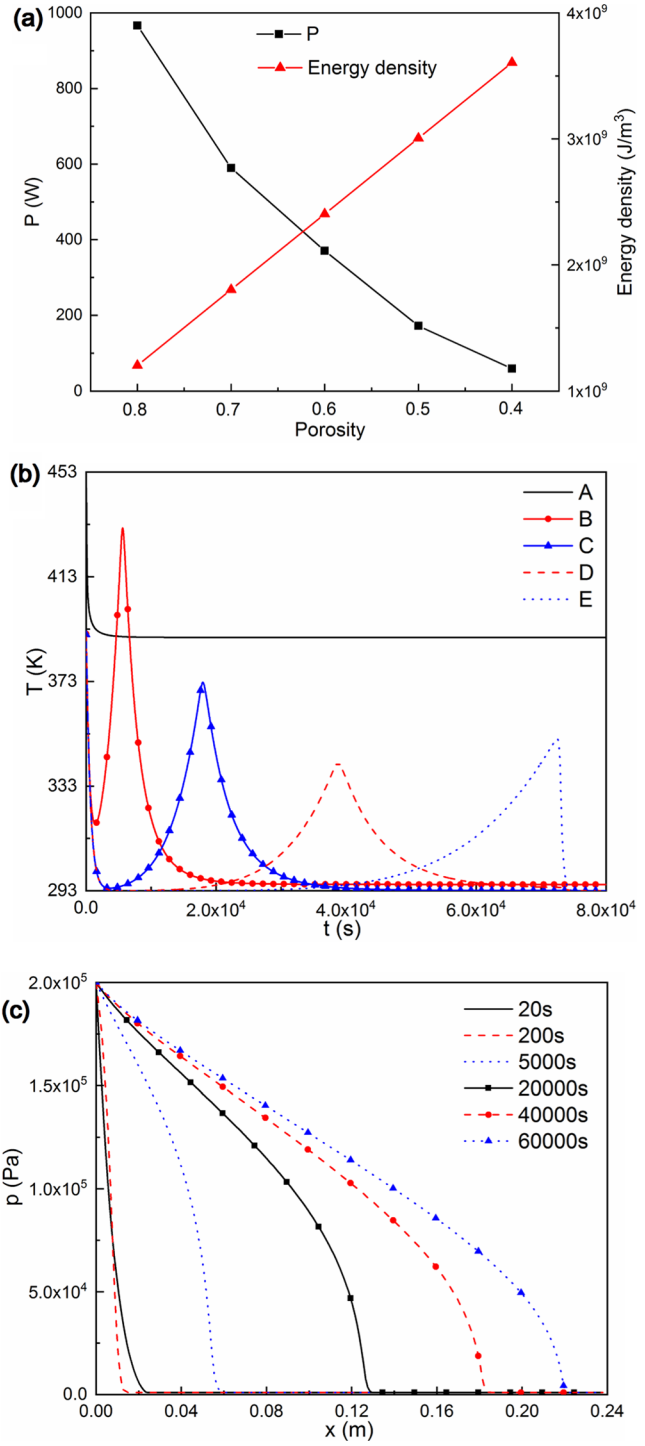
(a)
P
Energy density
P (W)
Energy density (J/m3)
Porosity
(b)
A
B
C
D
E
T (K)
t (s)
(c)
20s
200s
5000s
20000s
40000s
60000s
p (Pa)
x (m)

Besides, the average thermal power of the reactor is calculated as ratio of the total amount of reaction heat to the total reaction time as below

$$P = \frac{Q_{\text{total}}}{t_{\text{toal}}} = \frac{c_{\text{ini}} \cdot V_{\text{total}} \cdot \Delta H}{t_{\text{toal}}} \tag{23}$$

where V_{total} is the total volume of the 3D reactor and t_{total} is the total reaction time. As shown in Fig. 9a, although the low porosity reaches relatively high volume energy density, the very long reaction time greatly reduces the average thermal power.

The distribution of temperature and pressure of the case with 0.4 porosity is shown in Figs. 9b–c. As shown in Fig. 9b, due to the low reaction rate and slow advance of the reaction, the temperature plateau distributes more separately and its value is much lower than the base case. In Fig. 9c, the pressure in the downstream region is much harder to recover compared with the base case. This is because the low porosity leads to low permeability and high flow resistance which impedes the flow of water vapor. The distribution of temperature and pressure indicates that the reaction is restricted to a narrow region and the reaction time is prolonged spontaneously.

3.5 Effects of the Permeability

With other conditions the same as the base case, the permeability of the solid reactants is varied from 2×10^{-12} m^2 to 4×10^{-12} m^2, 2×10^{-11} m^2, 2×10^{-10} m^2, 2×10^{-9} m^2, 2×10^{-8} m^2, respectively. In practice, this can be achieved by changing the particle size while keeping the porosity constant. As shown in Table 2, the corresponding particle diameter ranges from 5 μm to 5 mm which is much less than the reactor diameter. Higher permeability means the water vapor can flow through the porous solid reactant more easily, rendering faster reaction rate. Thus, the reaction time decreases as the permeability increases as shown in Table 2. However, the reaction time hardly decreases when the permeability is larger than 2×10^{-10} m^2. When the permeability increases to 2×10^{-6} m^2, the reaction time (881 s) is only 3 s shorter than the case with permeability of 2×10^{-10} m^2 (884 s). This means acceleration of reaction rate by promotion of the fluid flow process is limited.

The distribution of temperature and pressure of the case with 2×10^{-10} m^2 permeability is shown in Fig. 10. The temperature plateaus of different observation points are in high coincidence, sustaining the same duration and reaching the same temperature plateau as shown in Fig. 10a. Besides, the maximum temperature in the reactor is higher than the base case and is closer to the equilibrium temperature of inlet pressure 200,000 Pa. This means the limitation of the hydration reaction is partly removed by the facilitated flow due to high permeability. In Fig. 10b, the pressure gradients at different times are very small compared with the base case. Thanks to the high permeability, water vapor can flow into the reactor with much lower resistance and provides adequate water vapor timely, thus allowing the hydration reaction to proceed synchronously in the whole reactor rather than in a restricted region. As shown in Fig. 10c, the velocity at 20 s is much higher than that of the base case in Fig. 6b due to the higher permeability. The distribution of velocity after the velocity peak is also more uniform compared with the base case.

It should be noted that when the permeability is higher than 2×10^{-10} m^2, it is found from the simulation that the maximum velocity of the water vapor varies from 1.004 ms^{-1} to 1.027 ms^{-1}, which is relatively high. In such case, the nonlinear (Forchheimer) drag force term may be required to be considered. The Ergun equation for the particle-packed porous media is as follows (Ergun 1952)

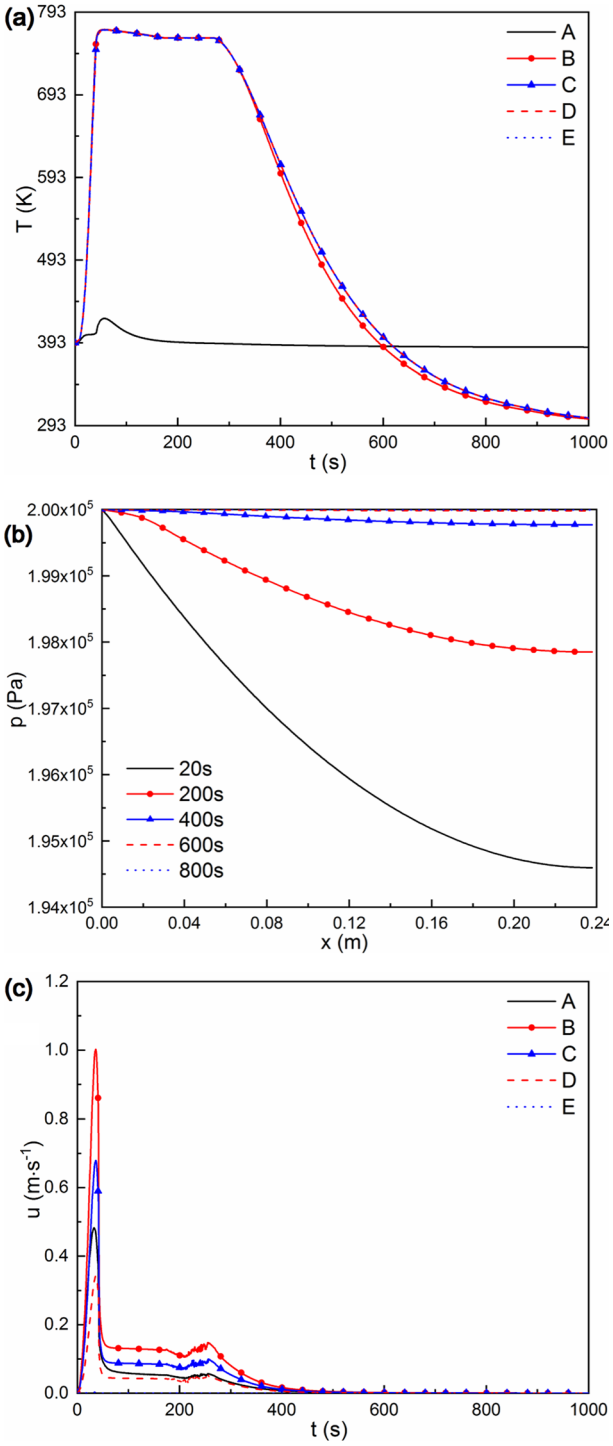

Fig. 10 Effects of the reactant permeability. **a** Temperature distribution of different observation points when the permeability is 2×10^{-10} m^2; **b** pressure distribution in the entire reactor at different times when the permeability is 2×10^{-10} m^2; **c** velocity distribution in the entire reactor of different observation points when the permeability is 2×10^{-10} m^2

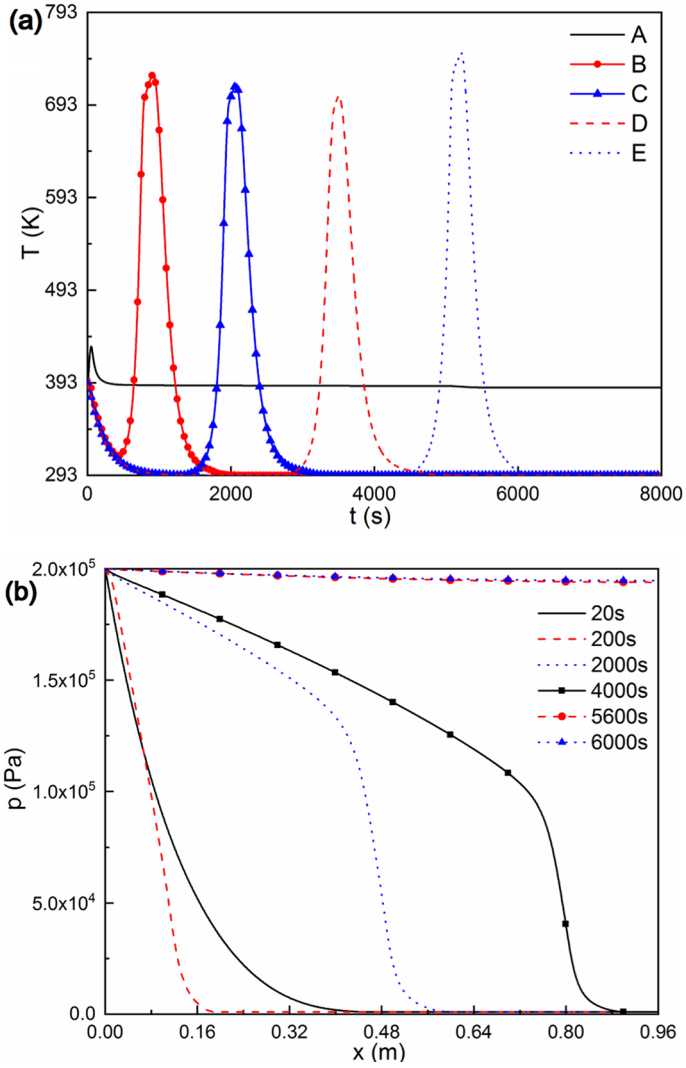

Fig. 11 Effects of the reactor length. **a** Temperature distribution of different observation points when the reactor length is 0.96 m; **b** pressure distribution in the entire reactor at different times when the reactor length is 0.96 m

$$\frac{|\Delta p|}{L} = \frac{\mu}{k}u + \frac{1.75\rho}{D_{\mathrm{p}}}\frac{(1-\varepsilon)}{\varepsilon^3}u^2 = C_1 \cdot u + C_2 \cdot u^2 \tag{24}$$

where the first term is the linear (Darcy) drag force term and the second term is the nonlinear drag force term. For the vapor flow studied in the present study, the value of C_2 is only about 0.1% of C_1, indicating that the second term at the right-hand side of Eq. (24) is much lower than the first term, and thus can be neglected.

3.6 Effects of the Reactor Size

The reactor size decides the amount of reactant and affects the heat and mass transfer processes. In this section, cases with different reactor lengths and diameters are investigated.

First, the reactor length is changed from 0.24 to 0.12 m, 0.48 m and 0.96 m, respectively, with other conditions the same as the base case. The reaction time shown in Table 2 increases linearly with increase in the reactor length due to proportional increase in the amount of reactant.

When the reactor length is 0.96 m, the vapor needs to flow longer distance from the upstream region to the downstream region rendering distribution of temperature plateaus scattered as shown in Fig. 11a. In Fig. 11b, sharp decrease in the pressure occurs in the downstream region at 2000s and 4000 s. This is because most of the water vapor has been consumed in the upstream region and has not reached the downstream region. The divisional reaction largely prolongs the reaction time.

Then, the reactor diameter is changed from 0.08 m to 0.04 m, 0.16 m and 0.32 m, respectively, with other conditions the same as the base case. The increase in the reactor diameter leads to increase in the reactant amount and prolongs the reaction time as shown in Table 2. According to Eq. (21), when the model is simplified to 1D, the increase in the reactor diameter reduces the convective heat transfer. Consequently, the heat released by hydration reaction cannot be removed timely and the hydration reaction is limited. However, the poor convection heat transfer increases the temperature which causes high reaction rate according to Eq. (4). The influence of these two factors is partly offset.

When the reactor diameter is 0.32 m, the distribution of the temperature plateau is more concentrated and the duration of temperature plateau is much longer than the base case as shown in Fig. 12a. The concentrated temperature plateau indicates the hydration reaction occurs uniformly in the entire reactor rather than in the local region. Consequently, the pressure inside the reactor can recover faster as shown in Fig. 12b. It is worth mentioning that considering the relatively high diameter–length ratio and the low thermal conductivity of reactants, the radial heat and mass transfer processes here need further consideration.

3.7 Effects of the Outlet Condition

In aforementioned cases, the boundary condition of the right bottom (the blue point in Fig. 1 is sealed adiabatic wall. The water vapor in the reactor can only be consumed by the hydration reaction or stays in the reactor. In several experiments (Criado et al. 2017; Pardo et al. 2014a; Schaube et al. 2013a), the reactors have outlet from which the unreacted water vapor can flow out. In this section, the right bottom is changed to the fully developed outlet with other conditions the same as the base case. The reaction time increases from 1500 to 1800s. The temperature of different observing points is shown in Fig. 13a. The temperature plateau appears successively as the reaction proceeds from the inlet to the outlet which is similar to the base case.

In Fig. 13b, the distribution of pressure at different times is also similar to the base case. The sequence of reaction in the upstream and the downstream regions leads to the intersection between 20 and 200 s. As reaction proceeds, the pressure drops quickly at 1000 s in the region near the outlet. This is mainly because the hydration reaction in this region consumes the water vapor and the fully developed outlet allows the vapor to flow out rather than accumulate inside the reactor. The lower pressure leads to decrease in the reaction rate

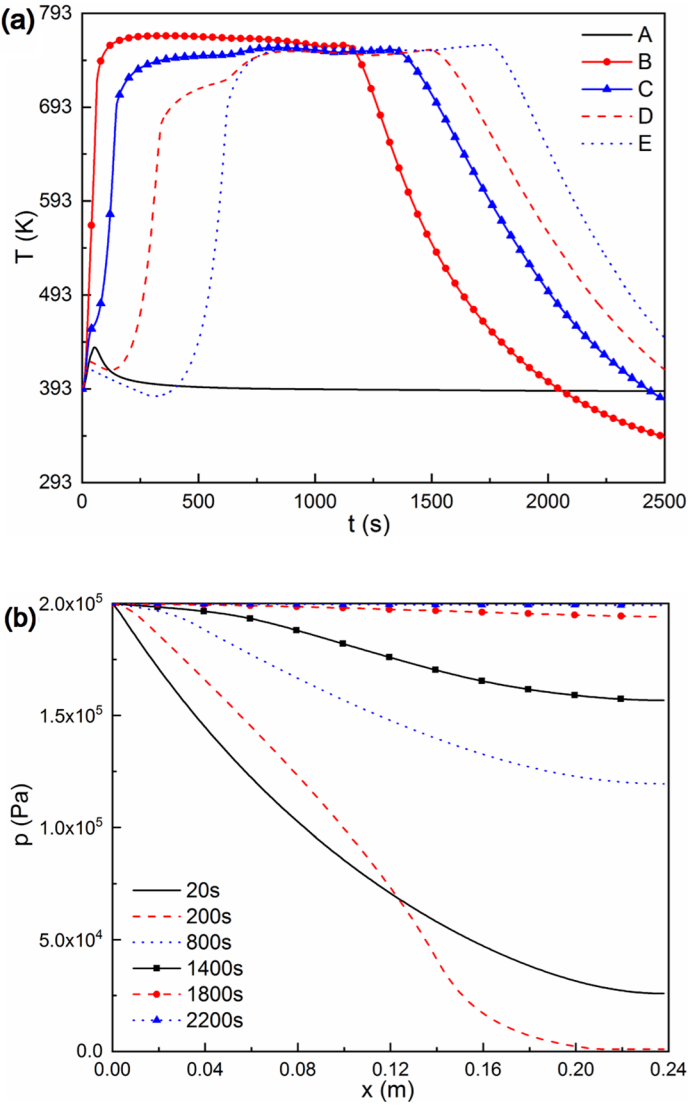

Fig. 12 Effects of the reactor diameter. **a** Temperature distribution of observation points when the reactor diameter is 0.32 m; **b** pressure distribution in the entire reactor at different times when the reactor diameter is 0.32 m

coefficient according to Eq. (4). Consequently, the reaction time is slightly prolonged to 1800s.

3.8 Comprehensive Analysis

The performance of cases with different conditions is evaluated with respect to the reaction time, average power, temperature plateau duration and standard deviation as shown

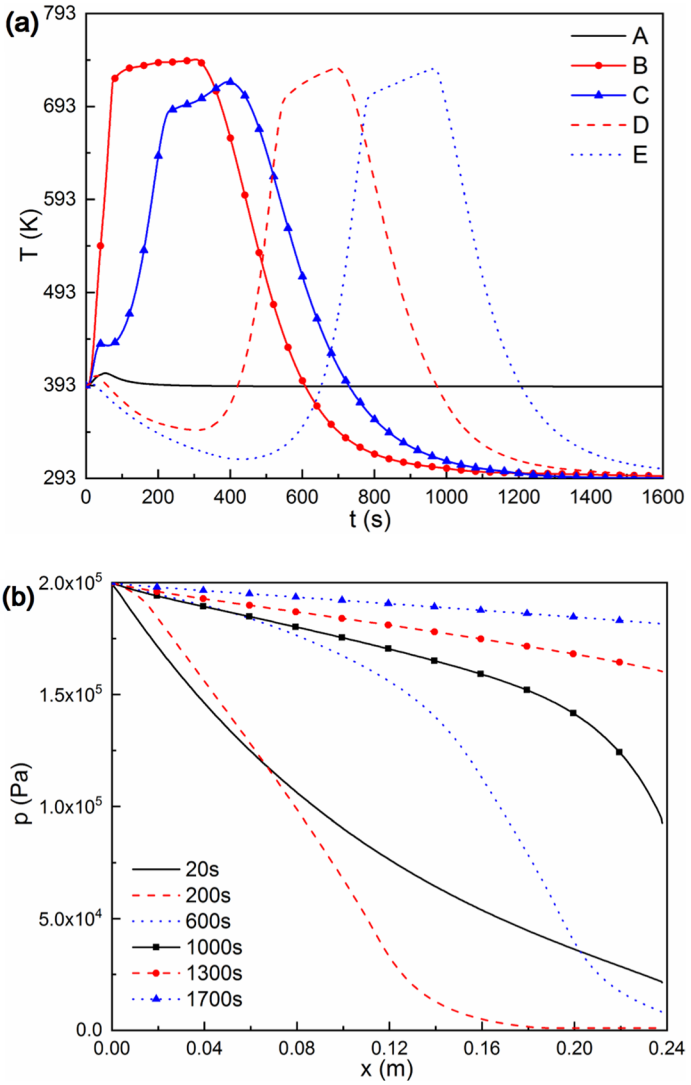

Fig. 13 Temperature and pressure of the case with fully developed outlet. **a** Temperature evolution of different observation points; **b** pressure distribution in the entire reactor at different times

in Fig. 14. The average power is calculated according to Eq. (23). Temperature plateau duration is the total duration time of the temperature plateau of different observation points in different cases and the overlapping part is not counted repeatedly. The midpoint of each temperature plateau of different observation points is utilized to calculate the standard deviation of different cases which can evaluate the reaction uniformity.

As shown in Fig. 14a, compared with the base case, higher inlet pressure, heat transfer coefficient and permeability, smaller reactor diameter and reactor length can shorten the reaction time. The average power of different cases is determined by the total amount of heat release as well as the reaction time as shown in Fig. 14b. With the same amount of

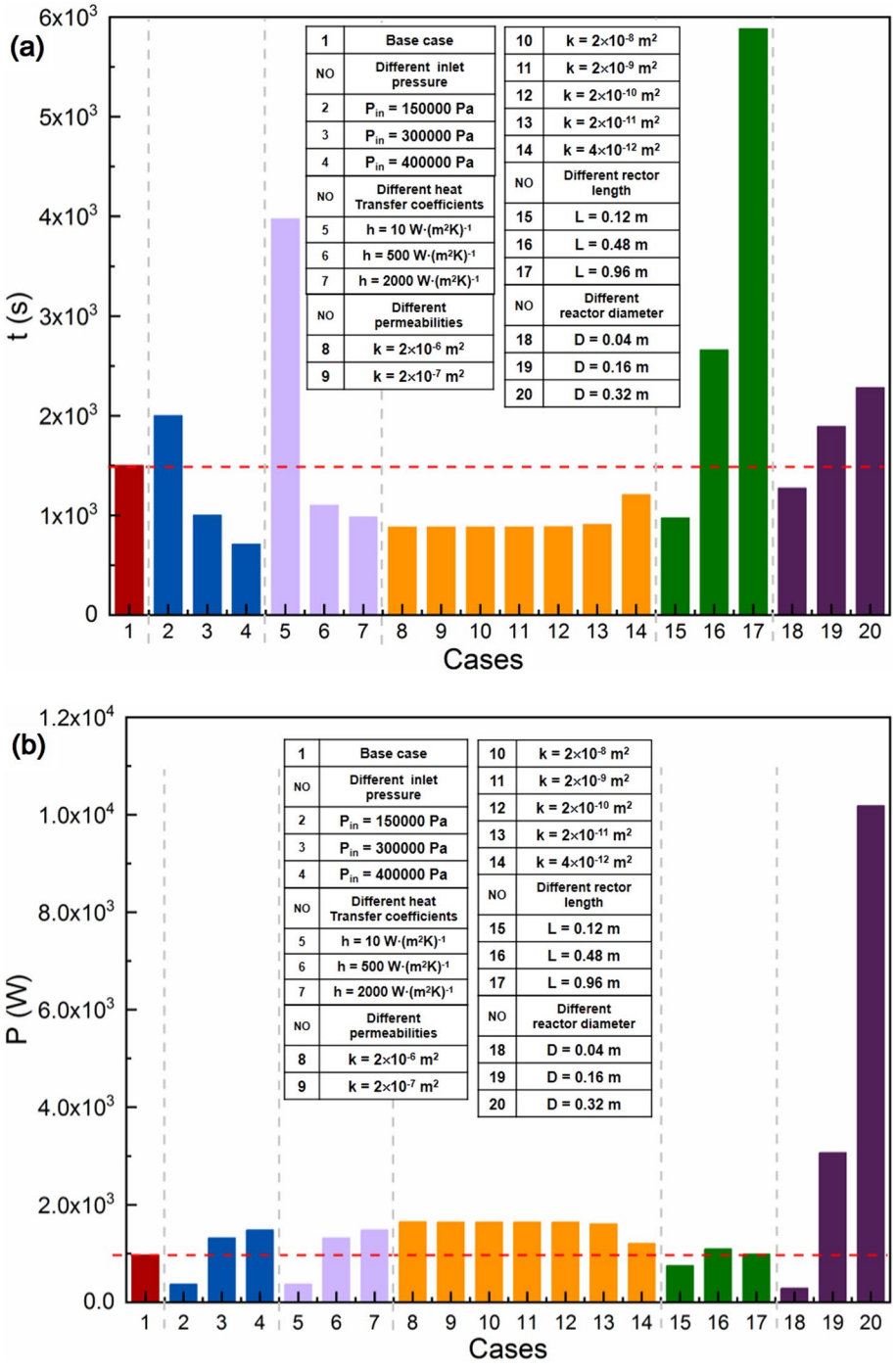

Fig. 14 Comparison between different cases. **a** Reaction rime; **b** average power; **c** temperature plateau duration; and **d** standard deviation of temperature plateau

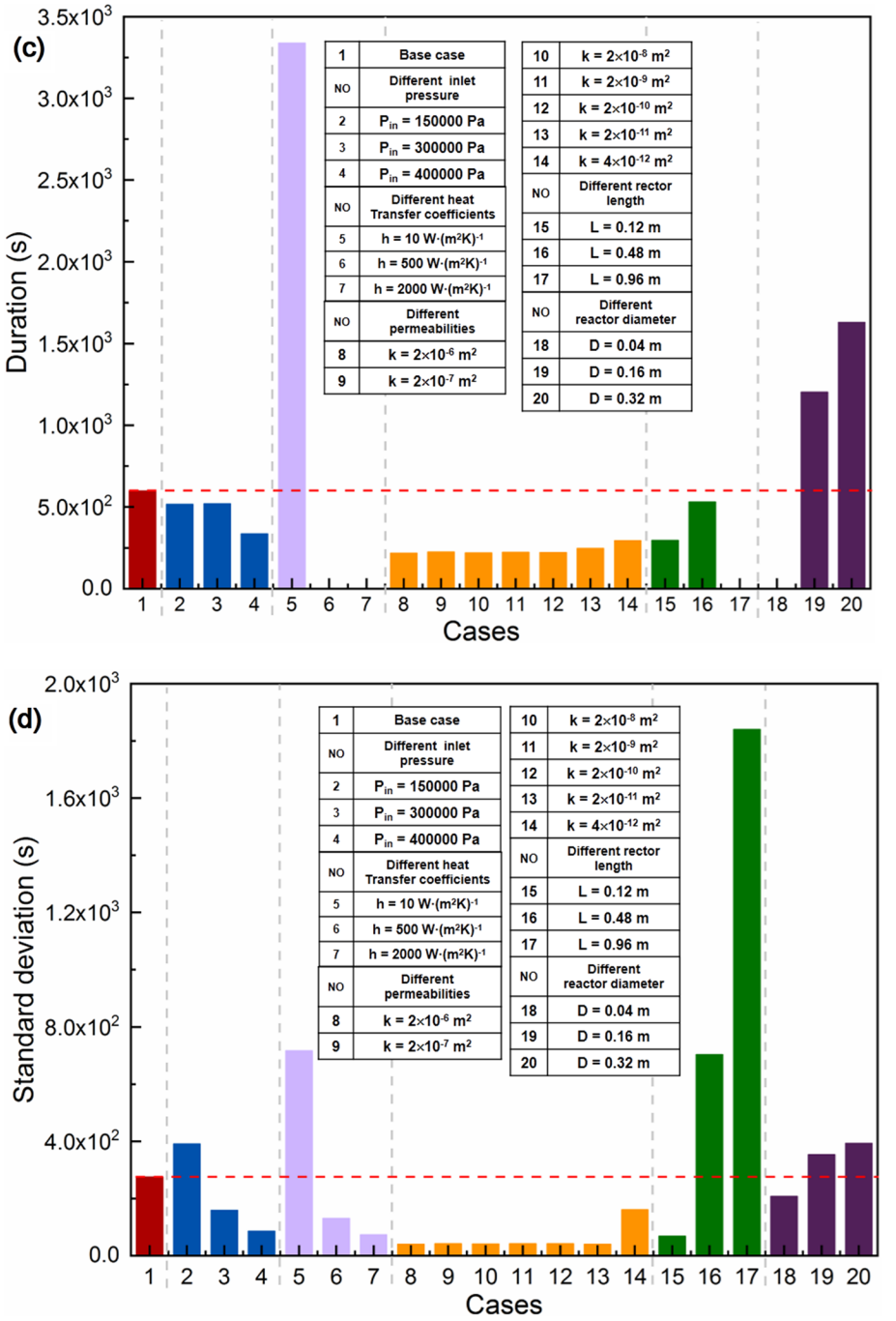

Fig. 14 (continued)

reactant CaO, when the inlet pressure (cases 2 to 4) and the heat transfer coefficient (cases 5 to 7) increase, the average power increases. The reaction time of cases with different permeability (cases 8–14) is similar; thus, the powers of these cases are also at similar level with same reactant amount. When the reactor length increases to 0.96 m (case 17), the reaction time is several times higher than the base case. However, the power is comparable to the base case due to the increase in the reactant amount. Even though reaction time increases when reactor diameter increases (cases 18 to 20), the increase in the amount of reactant ensures the relatively high power. The reaction time, the amount of heat and the average power can be controlled by designing the reactor size and choosing proper reaction conditions.

The temperature plateau duration and standard deviation are shown in Fig. 14c and d. Compared with the base case, the increase in the inlet pressure (cases 3 and 4) causes shorter duration due to decrease in the reaction time and less standard deviation, indicating more uniform reaction. When the convective heat transfer coefficient increases to 500 W m^{-2} K^{-1} (case 6) and further to 2000 W m^{-2} K^{-1} (case 7), the temperature decreases due to the strong convection and there is no obvious temperature plateau and the standard deviation is also relatively low. Cases with higher permeability (cases 8 to 14) show short temperature plateau duration and low standard deviation which is corresponding to the short reaction time and coincident temperature distribution discussed in Sect. 3.5. When the length increases to 0.96 m (case 17), there is no temperature plateau duration and the standard deviation is very high due to the partitioned reaction discussed in Sect. 3.6. When the reactor diameter is 0.04 m (case 18), the temperature plateau duration is 0 s due to the short reaction time. As the reactor diameter increases, the temperature plateau duration and the standard deviation increase mainly due to the prolonged reaction time. It can be indicated that more uniform reaction is faster and the temperature plateau is more concentrated with shorter duration.

4 Conclusions and Outlook

The coupled heat and mass transport reactive process during the hydration reaction of the $CaO/Ca(OH)_2$ thermochemical system is simulated in an indirect fixed bed with a 1D model. The main conclusions are summarized as follows:

(1) The reaction proceeds from inlet into the reactor and there will be a period of local stable reaction where there is a temperature plateau due to the equilibrium between the exothermic hydration reaction and convective heat transfer.
(2) Increasing the inlet pressure and strengthening the outside convective heat transfer can accelerate the reaction efficiently. The increase in the reactant permeability (constant porosity, larger particle diameter) enhances the reaction in a limited range. Decreasing the reactant porosity (constant particle diameter, lower permeability) leads to higher energy density, but longer reaction time.
(3) Increasing the reactor length prolongs the reaction time, and the average thermal power is comparable to that of the base case. Increasing the reactor diameter also prolongs the reaction time, but the average thermal power rises markedly.
(4) The efficient heat and mass transfer processes not only ensure fast reaction rate and high average thermal power, but also realize uniform reaction.

So far, the experimental and numerical simulation studies of the $CaO/Ca(OH)_2$ system are mainly in laboratory scale and have not been scaled up to the practical energy system. It still needs further investigation on the system operation and control to achieve application to industrial and civil field. The 1D model provides more detailed information of the complex reaction processes than the entire black box model and is simpler than the 2D and 3D model. Thus, it can be integrated into the practical energy system. Moreover, the reaction characteristics are closely associated with the microgeometry of the reactants as well as the heat and mass transfer processes in the porous media. It is essential to develop the microscale model and explore the underlying reaction mechanism. These studies are undergoing in our group.

Acknowledgements The authors thank the support of National Nature Science Foundation of China (51776159), Shaanxi Province Science Fund for Distinguished Young Scholars (2019JC-01), the Fundamental Research Funds for the Central Universities, the Foundation for Innovative Research Groups of the National Natural Science Foundation of China (No. 51721004) and 111 Project (B16038). We also appreciate the anonymous reviewers for their helpful comments, which greatly improve our work.

Compliance with Ethical Standards

Conflict of interest The authors declare that they have no conflict of interest.

References

Carrillo, A.J., Gonzalez-Aguilar, J., Romero, M., Coronado, J.M.: Solar energy on demand: a review on high temperature thermochemical heat storage systems and materials. Chem. Rev. **119**(7), 4777–4816 (2019). https://doi.org/10.1021/acs.chemrev.8b00315

Cosquillo Mejia, A., Afflerbach, S., Linder, M., Schmidt, M.: Experimental analysis of encapsulated $CaO/Ca(OH)_2$ granules as thermochemical storage in a novel moving bed reactor. Appl. Therm. Eng. (2020). https://doi.org/10.1016/j.applthermaleng.2020.114961

Criado, Y.A., Alonso, M., Abanades, J.C.: Kinetics of the $CaO/Ca(OH)_2$ hydration/dehydration reaction for thermochemical energy storage applications. Ind. Eng. Chem. Res. **53**(32), 12594–12601 (2014). https://doi.org/10.1021/ie404246p

Criado, Y.A., Huille, A., Rougé, S., Abanades, J.C.: Experimental investigation and model validation of a $CaO/Ca(OH)_2$ fluidized bed reactor for thermochemical energy storage applications. Chem. Eng. J. **313**, 1194–1205 (2017). https://doi.org/10.1016/j.cej.2016.11.010

Darcy, H.: Les Fontains Publiques de la Ville de Dijon. Paris (1956)

Darkwa, K., Ianakiev, A., O'Callaghan, P.W.: Modelling and simulation of adsorption process in a fluidised bed thermochemical energy reactor. Appl. Therm. Eng. **26**(8–9), 838–845 (2006). https://doi.org/10.1016/j.applthermaleng.2005.10.008

Ergun, S.: Fluid flow through packed columns. Chem. Eng. Prog. **48**(2), 6 (1952)

Herrmann, U., Kearney, D.W.: Survey of thermal energy storage for parabolic troughpower plants. J. Solar Energy Eng. **124**, 145–152 (2002). https://doi.org/10.1115/1.1467601 (兴)

Kugeler, K., Niessen, H.F., Röth-Kamat, M., Böcker, D., Rüter, B., Theis, K.A.: Transport of nuclear heat by means of chemical energy (nuclear long-distance energy). Nucl. Eng. Des. **34**(1), 65–72 (1975). https://doi.org/10.1016/0029-5493(75)90156-9

Linder, M., Roßkopf, C., Schmidt, M., Wörner, A.: Thermochemical energy storage in kW-scale based on $CaO/Ca(OH)_2$. Energy Proc. **49**, 888–897 (2014). https://doi.org/10.1016/j.egypro.2014.03.096

Nagel, T., Shao, H., Singh, A.K., Watanabe, N., Roßkopf, C., Linder, M., Wörner, A., Kolditz, O.: Non-equilibrium thermochemical heat storage in porous media: part 1—Conceptual model. Energy **60**, 254–270 (2013). https://doi.org/10.1016/j.energy.2013.06.025

Pan, Z.H., Zhao, C.Y.: Gas–solid thermochemical heat storage reactors for high-temperature applications. Energy **130**, 155–173 (2017). https://doi.org/10.1016/j.energy.2017.04.102

Pardo, P., Anxionnaz-Minvielle, Z., Rougé, S., Cognet, P., Cabassud, M.: $Ca(OH)_2$/CaO reversible reaction in a fluidized bed reactor for thermochemical heat storage. Sol. Energy **107**, 605–616 (2014a). https://doi.org/10.1016/j.solener.2014.06.010

Pardo, P., Deydier, A., Anxionnaz-Minvielle, Z., Rougé, S., Cabassud, M., Cognet, P.: A review on high temperature thermochemical heat energy storage. Renew. Sustain. Energy Rev. **32**, 591–610 (2014b). https://doi.org/10.1016/j.rser.2013.12.014

Ranjha, Q., Oztekin, A.: Numerical analyses of three-dimensional fixed reaction bed for thermochemical energy storage. Renew. Energy **111**, 825–835 (2017). https://doi.org/10.1016/j.renene.2017.04.062

Roßkopf, C., Afflerbach, S., Schmidt, M., Görtz, B., Kowald, T., Linder, M., Trettin, R.: Investigations of nano coated calcium hydroxide cycled in a thermochemical heat storage. Energy Convers. Manag. **97**, 94–102 (2015). https://doi.org/10.1016/j.enconman.2015.03.034

Schaube, F., Wörner, A., Tamme, R.: High temperature thermochemical heat storage for concentrated solar power using gas–solid reactions. J. Solar Energy Eng. **133**, 7 (2011). https://doi.org/10.1115/1.4004245

Schaube, F., Koch, L., Wörner, A., Müller-Steinhagen, H.: A thermodynamic and kinetic study of the de- and rehydration of $Ca(OH)_2$ at high H_2O partial pressures for thermo-chemical heat storage. Thermochim. Acta **538**, 9–20 (2012). https://doi.org/10.1016/j.tca.2012.03.003

Schaube, F., Kohzer, A., Schütz, J., Wörner, A., Müller-Steinhagen, H.: De- and rehydration of Ca(OH)2 in a reactor with direct heat transfer for thermo-chemical heat storage. Part A: experimental results. Chem. Eng. Res. Des. **91**(5), 856–864 (2013a). https://doi.org/10.1016/j.cherd.2012.09.020

Schaube, F., Utz, I., Wörner, A., Müller-Steinhagen, H.: De- and rehydration of Ca(OH)2 in a reactor with direct heat transfer for thermo-chemical heat storage. Part B: Validation of model. Chem. Eng. Res. Des. **91**(5), 865–873 (2013b). https://doi.org/10.1016/j.cherd.2013.02.019

Schmidt, M., Linder, M.: Power generation based on the $Ca(OH)_2$/CaO thermochemical storage system—Experimental investigation of discharge operation modes in lab scale and corresponding conceptual process design. Appl. Energy **203**, 594–607 (2017). https://doi.org/10.1016/j.apenergy.2017.06.063

Schmidt, M., Szczukowski, C., Roßkopf, C., Linder, M., Wörner, A.: Experimental results of a 10 kW high temperature thermochemical storage reactor based on calcium hydroxide. Appl. Therm. Eng. **62**(2), 553–559 (2014). https://doi.org/10.1016/j.applthermaleng.2013.09.020

Schmidt, M., Gutierrez, A., Linder, M.: Thermochemical energy storage with CaO/$Ca(OH)_2$—Experimental investigation of the thermal capability at low vapor pressures in a lab scale reactor. Appl. Energy **188**, 672–681 (2017). https://doi.org/10.1016/j.apenergy.2016.11.023

Sebarchievici, I.S.C.: A comprehensive review of thermal energy storage. Sustainability (2018). https://doi.org/10.3390/su10010191

Seitz, G., Helmig, R., Class, H.: A numerical modeling study on the influence of porosity changes during thermochemical heat storage. Appl. Energy (2020). https://doi.org/10.1016/j.apenergy.2019.114152

Shao, H., Nagel, T., Roßkopf, C., Linder, M., Wörner, A., Kolditz, O.: Non-equilibrium thermo-chemical heat storage in porous media: part 2—A 1D computational model for a calcium hydroxide reaction system. Energy **60**, 271–282 (2013). https://doi.org/10.1016/j.energy.2013.07.063

Sunku Prasad, J., Muthukumar, P., Desai, F., Basu, D.N., Rahman, M.M.: A critical review of high-temperature reversible thermochemical energy storage systems. Appl. Energy (2019). https://doi.org/10.1016/j.apenergy.2019.113733

Wang, M., Chen, L., He, P., Tao, W.: Numerical study and enhancement of $Ca(OH)_2$/CaO dehydration process with porous channels embedded in reactors. Energy **181**, 417–428 (2019). https://doi.org/10.1016/j.energy.2019.05.184

Wood, D.A.: The natural gas sector needs to be mindful of its sustainability credentials. Adv. Geoenergy Res. **4**(3), 229–232 (2020). https://doi.org/10.46690/ager.2020.03.01

Xu, J., Wang, R.Z., Li, Y.: A review of available technologies for seasonal thermal energy storage. Sol. Energy **103**, 610–638 (2014). https://doi.org/10.1016/j.solener.2013.06.006

Yadav, D., Banerjee, R.: A review of solar thermochemical processes. Renew. Sustain. Energy Rev. **54**, 497–532 (2016). https://doi.org/10.1016/j.rser.2015.10.026

Yan, J., Zhao, C.Y.: Experimental study of CaO/$Ca(OH)_2$ in a fixed-bed reactor for thermochemical heat storage. Appl. Energy **175**, 277–284 (2016). https://doi.org/10.1016/j.apenergy.2016.05.038

Yu, G., Jia, S., Dai, B.: Review on recent liquefied natural gas cold energy utilization in power generation cycles. Adv. Geoenergy Res. **2**(1), 86–102 (2018). https://doi.org/10.26804/ager.2018.01.08